A comprehensive study on physics-based simulation combined multi-objective optimization of capacity decay and voltage loss of Vanadium redox flow battery

Liezhi Lu[a], Ana Jorge Sobrido[b], Liang Gao[a], Akhil Garg[a,*], Wei Li[c]

[a]School of Mechanical Science and Engineering, Huazhong University of Science and Technology, Wuhan, China
[b]Materials Research Institute, Queen Mary University of London, London, UK
[c]School of Mechanical Engineering, Hefei University of Technology, Hefei, China

Abstract

This paper proposes physics-based simulation combined multi-objective optimization approach for reduction of both capacity decay and voltage loss of Vanadium redox flow battery. In this approach, firstly, a physics-based-electrochemical model for a single-cell VRFB is developed based on the dynamic plug flow reactor model and is used to obtain capacity decay and voltage loss under various conditions. Simulation studies were then conducted to investigate the effects of electrolyte flow rate and electrode fiber diameter on the VRFB performance. The capacity decay in VRFB relies mainly on the vanadium ions' variation between two half-cells. The variation in the long-term cycle is fundamentally due to the electrolyte transfer across the membrane. The lower electrolyte flow rate, as well as electrode fiber diameter, can reduce the capacity decay as the electrolyte's velocity across the membrane decreases. However, the lower electrolyte flow rate and electrode fiber diameter increase the voltage loss considering open circuit voltage loss, activation overpotential, and concentration overpotential. Finally, a novel optimization framework combined with simulation and the meta-heuristic algorithm is introduced to reduce both capacity decay and voltage loss in VRFB simultaneously. The proposed multi-objective method shows a significant reduction of both capacity decay and voltage loss.

Keywords: Vanadium redox flow battery, Electrolyte flow rate, Electrode fiber diameter, Electrochemical simulation, Heuristic algorithm, Pareto optimality

1. Introduction

Vanadium redox flow battery (VRFB), first developed by Skyllas-Kazacos et al.[1, 2] in the 1980s, is the most mature flow battery technology[3]. VRFB adopts vanadium in both half cells, avoiding cross-contamination caused by electrolyte diffusion between half cells[4]. Moreover, two separate electrolyte storage tanks are applied to store energy in VRFB. Therefore, the capacity of VRFB can be easily extended by increasing electrolyte volume in the tank[5]. Because of the above characteristics, VRFB is considered one of the most promising grid-scale electrochemical energy storage technologies[4]. Furthermore, the advantages of this technology have been demonstrated in several commercial systems[6].

Efficiency and capacity are two equally essential metrics in VRFB. Efficiency is primarily related to cycle performance. Moreover, low efficiency indirectly increases the capital cost of manufacturing cell stacks[7]. The capacity significantly affects the long-term stability of the VRFB and the costs associated with operation and maintenance[8, 9, 10]. Therefore, an effective way to improve VRFB performance is to improve cell efficiency and reduce capacity loss.

Faraday's law of electrolysis indicates that changes in reactant concentration and electrolyte volume can lead to capacity decay. Numerous studies have developed mathematical models to analyze and quantify capacity decay based on ion diffusion and electrolyte transfer[11, 12, 13, 14, 15, 16, 17, 18]. The results show that a lower electrolyte flow rate corresponds to less capacity decay. Additionally, a lower electrolyte flow rate can result in a higher concentration overpotential which in turn harms battery efficiency[11, 19, 20]. Therefore, it is essential to consider both voltage loss and capacity decay when optimizing the electrolyte flow rate.

However, many existing experimental and model-based approaches optimize the electrolyte flow rate based on either voltage loss or capacity decay. For example, Ma et al.[21] successfully reduced capacity decay by applying various constant flow rates at predetermined voltage levels and conducting experiments on an actual battery stack of 15 cells to determine the optimal flow rate control strategy. Christian et al.[22] proposed a new flow control strategy that enhanced the energy efficiency of the battery by taking advantage of the knowledge of the VRFB operating principles provided by the multi-physics model. Tang et al.[23] modeled the concentration overpotential as a function of flow rate to determine the electrolyte flow rate that results in high system efficiency. Xiong et al.[24] developed an electrochemical model based on experimental data and optimized the electrolyte flow rate with an empirical approach.

Meanwhile, only a handful of studies have simultaneously considered electrolyte flow rate's effect on voltage loss and capacity decay. König et al. [25] based on a multi-physics battery model to obtain the optimal flow rate at the operating

*Corresponding author. Email-address: akhilgarg@hust.edu.cn

point, which increased the discharge capacity while minimizing the concentration overpotential in VRFB. Khaki et al. [26] transformed the multi-objective problem into a single-objective problem by assigning weights to voltage losses and capacity decay and then combined this with a zero-dimensional electrochemical model to obtain the optimal electrolyte flow rate.

In the above studies, the experiment-based approach requires many experiments, which takes considerably more time compared to the model-based approach. Model-based approaches have become the focus of current research due to their high efficiency. Accurate modeling of the VRFB is a vital part of the model-based approach. Among all the mathematical models of VRFB, the zero-dimensional model not only considers enough electrochemical details but also has a more direct definition than other high-dimensional models. Therefore, this model has been used extensively in the literature to analyze the performance of VRFBs [5, 25, 26]. Accordingly, a modified zero-dimensional model extended from the dynamic plug flow reactor model proposed in[5] is employed in this study.

Besides, most of the above studies take no account of the transfer of electrolytes between half cells. Moreover, they only consider the effect of electrolyte flow rate on voltage loss and capacity decay. However, electrode fiber diameter is also an essential factor affecting the performance of VRFB. Therefore, given the shortcomings of the above research, this study has made the following contributions:

- An electrochemical model based on the dynamic plug flow reactor is developed. It considers not only the influence of the electrolyte flow rate but also the influence of the electrode fiber diameter on the performance of VRFB.
- Based on the existing research, the capacity decay and voltage loss are accurately modelled. Moreover, this study defines a more precise expression of capacity decay and voltage loss through simulation analysis.
- A novel optimization framework based on Pareto optimality combined with simulation and the meta-heuristic algorithm is introduced in this study to obtain the Pareto frontier. Compared to the method of converting multiple objectives into a single objective by using assigned weights, this framework is able to accurately find the objectively better solution. Also, solutions with different ratios are provided for specific needs.
- The use of simulation combined with meta-heuristic algorithms allows us to optimize the VRFB from the parameter design stage. We have considered both the design parameter (electrode fibre diameter) and the operating parameter (electrolyte flow rate) of the VRFB in terms of their effect on capacity decay and voltage loss.

2. Model development

2.1. Assumptions and simplifications

1. Cell and electrolyte temperatures are maintained at 25 °C.
2. Oxygen and hydrogen evolutions are neglected.
3. The electrolyte in half-cells and tanks is perfectly mixed.
4. The resistivity of VRFB remains constant.
5. Self-discharge reaction caused by vanadium ion diffusion is instantaneous.
6. Electrolyte transmembrane transfer is instantaneous.
7. Electrodes with different electrode fiber diameters have the same porosity.
8. Neglecting electrolyte density changes caused by electrolyte transfer.
9. The transfer of hydrogen ions between half-cells is not considered.

2.2. Capacity decay of VRFB

Capacity decay in VRFB is closely related to the concentration of vanadium ions in positive and negative tanks. Therefore, accurate modeling of ion concentration changes in storage tanks and half-cells is critical. There are three primary sources of vanadium ion concentration variation in VRFB: ion redox reaction during battery charge and discharge, self-discharge reaction caused by ion transmembrane diffusion, and transmembrane transfer of electrolyte.

In VRFB, V^{2+}/V^{3+} and V^{4+}/V^{5+} are used as redox pairs of cathode and anode, respectively. The following equations can describe the redox reaction of VRFB during charging and discharging:

At the negative electrode:

$$\mathrm{V^{3+} + e^- \underset{\text{discharge}}{\overset{\text{charge}}{\rightleftharpoons}} V^{2+}},\ E^0 = -0.26V \tag{1}$$

At the positive electrode:

$$\mathrm{VO^{2+} + H_2O \underset{\text{discharge}}{\overset{\text{charge}}{\rightleftharpoons}} VO_2^{+} + 2\,H^+ + e^-},\ E^0 = +1.00V \tag{2}$$

Ideally, only protons can pass through the ion exchange membrane to balance the positive and negative half-cells during charging and discharging. However, there exists a pressure difference between the positive and negative half-cells. Furthermore, the membrane is permeable to the electrolyte. Therefore, the phenomenon of electrolyte transmembrane transfer occurs.

The self-discharge reaction occurs when vanadium ions diffuse from one half-cell to the other. It results in an imbalance of vanadium ions between the half cells, which reduces the battery capacity. The self-discharge reaction of the positive and negative half-cells are shown as follows[12]:

At the negative electrode:

$$\begin{aligned} &\mathrm{VO^{2+} + V^{2+} + 2\,H^+ \longrightarrow 2\,V^{3+} + H_2O} \\ &\mathrm{VO_2^{+} + 2\,V^{2+} + 4\,H^+ \longrightarrow 3\,V^{3+} + 2\,H_2O} \\ &\mathrm{VO_2^{+} + V^{3+} \longrightarrow 2\,VO^{2+}} \end{aligned} \tag{3}$$

At the positive electrode:

$$\begin{aligned} &\mathrm{V^{2+} + 2\,VO_2^{+} + 2\,H^+ \longrightarrow 3\,VO^{2+} + H_2O} \\ &\mathrm{V^{3+} + VO_2^{+} \longrightarrow 2\,VO^{2+}} \\ &\mathrm{V^{2+} + VO^{2+} \longrightarrow 2\,V^{3+} + H_2O} \end{aligned} \tag{4}$$

The electrolyte transfer from one half-cell to the other will cause volume differences between half-cells. Therefore, it is necessary to consider the effect of volume difference on VRFB performance. This study assumes that the volume loss in half-cells will be immediately replenished from tanks. Therefore, this study does not consider the effect of volume loss on the reaction in the half-cells.

The partial differential equation (PDE) based on material balance is transformed into an ordinary differential equation (ODE) by discretizing VRFB Only the concentration change in the vertical direction of half-cells is considered. This study divides the half-cell into N layers, and the ion concentration change of the k^{th} layer can be expressed by Eq. (5)[5]. where L_{pe}, W_{pe} and H_{pe} represent the geometry of the electrode, $c^{cell}_{i,k}(i = 2, .., 5)$ represent the states of ion concentration in the kth layer, Q is the electrolyte flow rate, $\frac{k_{id}}{d}(i = 2, ..., 5)$ represent the diffusion coefficient of vanadium species, and I is the input current ($I > 0$ for charging and $I < 0$ for discharging).

The ion concentration change in the tanks can be expressed as follows:

$$\begin{aligned}
\frac{dc_2^{tank}(t)}{dt} &= \frac{\left(c^{cell}_{2,N}(t) - c_2^{tank}(t)\right)Q}{V^-_{tank}} + \Delta c_2 \\
\frac{dc_3^{tank}(t)}{dt} &= \frac{\left(c^{cell}_{3,N}(t) - c_3^{tank}(t)\right)Q}{V^-_{tank}} + \Delta c_3 \\
\frac{dc_4^{tank}(t)}{dt} &= \frac{\left(c^{cell}_{4,N}(t) - c_4^{tank}(t)\right)Q}{V^+_{tank}} + \Delta c_4 \\
\frac{dc_5^{tank}(t)}{dt} &= \frac{\left(c^{cell}_{5,N}(t) - c_2^{tank}(t)\right)Q}{V^+_{tank}} + \Delta c_5
\end{aligned} \tag{6}$$

where $c_i^{tank}(i = 2, .., 5)$ represent the states of ion concentration in tanks and $\Delta c_i(i = 2, .., 5)$ are the modification for ion concentration due to volume loss which can be expressed as follows:

$$\begin{aligned}
\Delta c_2 &= c_2^{tank}(t) \times \frac{-\Delta V^-}{V^-_{tank}(t) + \Delta V^-} \\
\Delta c_3 &= c_3^{tank}(t) \times \frac{\Delta V^-}{V^-_{tank}(t) + \Delta V^-} \\
\Delta c_4 &= c_4^{tank}(t) \times \frac{-\Delta V^+}{V^+_{tank}(t) + \Delta V^+} \\
\Delta c_5 &= c_5^{tank}(t) \times \frac{-\Delta V^+}{V^+_{tank}(t) + \Delta V^+}
\end{aligned} \tag{7}$$

where V^+_{tank}/V^-_{tank} represents the remaining electrolyte volume in the positive and negative tanks respectively, $\Delta V^+/\Delta V^-$ represent the volume loss for the positive and negative tanks respectively. According to [27], $\Delta V^+/\Delta V^-$ can be modelled as described by the following equation:

$$\Delta V^+ = -\Delta V^+ = \vec{v}_m S_m \Delta t \tag{8}$$

where S_m is the membrane surface area, $\vec{v}_m$ is the velocity of the electrolyte across the membrane. According to [26], it can be derived from the following equation:

$$\vec{v}_m = \frac{\kappa_m A_m}{\mu^- \theta} \frac{H_{pe} Q}{2\kappa_{pe} A_{cs}} (\mu^- - \mu^+) \tag{9}$$

where κ_m and θ represent the permeability and thickness of the membrane individually, A_m is the membrane area, A_{cs} is the cross-sectional area of the electrode, μ^+/μ^- represent the viscosity of electrolyte in anode and cathode individually, and κ_{pe} is the permeability of the electrode which can be derived from Tamayol-Bahrami model[28]:

$$\kappa_{pe} = 0.012\epsilon d_f^2 \tau \left[\left(\frac{\pi}{4(1-\epsilon)}\right)^2 - \frac{\pi}{2(1-\epsilon)} + 1\right] \tag{10}$$

where ϵ is the porosity of the electrode, d_f is the electrode fiber diameter, and τ is the tortuosity factor correlated with ϵ as the following[29]:

$$\tau = \left[1 + 0.72\frac{1-\epsilon}{(\epsilon - 0.11)^{0.54}}\right] \tag{11}$$

According to [30], μ^+/μ^- is closely related to the composition of electrolyte in half-cells. And they can be expressed as Eq. (11) where δ^+/δ^- represents the proportion of solvent in electrolyte.

$$\begin{aligned}
\mu^- &= f(c_2(t), c_3(t), \delta^-) \\
\mu^+ &= f(c_4(t), c_5(t), \delta^+)
\end{aligned} \tag{12}$$

2.3. Voltage loss of VRFB

In general, the terminal voltage E_t can be obtained from Nernst equation, as shown in Eq. (13). The last item contains three main sources of voltage loss in VRFB: ohmic drop ir, concentration overpotential η_c^+/η_c^-, and activation overpotential η_a^+/η_a^-.

$$E_t = E_{OCV} + sign(I)(ir + \eta_c^+ + \eta_c^- + \eta_a^+ + \eta_a^-) \tag{13}$$

As shown in Eq. (14), Li[5] employ a new formal potential term which has been reported as $E_0' = 1.4V$ by Corcuera and Skyllas-Kazacos[31] to simplify the calculation of the open circuit voltage E_{OCV}.

$$E_{OCV} = E_0' + \frac{RT}{nF} \ln\left(\frac{c^{cell}_{2,mean} c^{cell}_{5,mean}}{c^{cell}_{3,mean} c^{cell}_{4,mean}}\right) \tag{14}$$

The vanadium ion concentration in the half-cells is uneven in the vertical direction because of discrete modeling of VRFB. Therefore, Eq. (14) uses the average ion concentration $c^{cell}_{i,mean}(i = 2, .., 5)$ in the half-cells to calculate E_{OCV}. The ohmic drop can be obtained by current density and battery resistivity. The concentration overpotential can be derived from the following equation[23, 26]:

At charging:

$$\eta_c = \eta_c^+ + \eta_c^- = \frac{RT}{nF}\left[\ln\left(\frac{c^{cell}_{3,mean} - \frac{i}{nFk_{3m}}}{c^{cell}_{3,mean}} \frac{c^{cell}_{4,mean} - \frac{i}{nFk_{4m}}}{c^{cell}_{4,mean}}\right)\right] \tag{15}$$

$$
\begin{aligned}
\frac{L_{pe}W_{pe}\Delta H_{pe}}{2}\frac{dc_{2,k}^{cell}(t)}{dt} &= \left[c_{2,k-1}^{cell}(t)-c_{2,k}^{cell}(t)\right]Q+sign(I)\frac{iL_{pe}\Delta H_{pe}}{nF}-k_{2d}\frac{c_{2,k}^{cell}(t)}{d}L_{pe}\Delta H_{pe}-2k_{5d}\frac{c_{5,k}^{cell}(t)}{d}L_{pe}\Delta H_{pe}-k_{4d}\frac{c_{4,k}^{cell}(t)}{d}L_{pe}\Delta H_{pe}\\
\frac{L_{pe}W_{pe}\Delta H_{pe}}{2}\frac{dc_{3,k}^{cell}(t)}{dt} &= \left[c_{3,k-1}^{cell}(t)-c_{3,k}^{cell}(t)\right]Q-sign(I)\frac{iL_{pe}\Delta H_{pe}}{nF}-k_{3d}\frac{c_{3,k}^{cell}(t)}{d}L_{pe}\Delta H_{pe}+3k_{5d}\frac{c_{5,k}^{cell}(t)}{d}L_{pe}\Delta H_{pe}+2k_{4d}\frac{c_{4,k}^{cell}(t)}{d}L_{pe}\Delta H_{pe}\\
\frac{L_{pe}W_{pe}\Delta H_{pe}}{2}\frac{dc_{4,k}^{cell}(t)}{dt} &= \left[c_{4,k-1}^{cell}(t)-c_{4,k}^{cell}(t)\right]Q-sign(I)\frac{iL_{pe}\Delta H_{pe}}{nF}-k_{4d}\frac{c_{4,k}^{cell}(t)}{d}L_{pe}\Delta H_{pe}+3k_{2d}\frac{c_{2,k}^{cell}(t)}{d}L_{pe}\Delta H_{pe}+2k_{3d}\frac{c_{3,k}^{cell}(t)}{d}L_{pe}\Delta H_{pe}\\
\frac{L_{pe}W_{pe}\Delta H_{pe}}{2}\frac{dc_{5,k}^{cell}(t)}{dt} &= \left[c_{5,k-1}^{cell}(t)-c_{5,k}^{cell}(t)\right]Q+sign(I)\frac{iL_{pe}\Delta H_{pe}}{nF}-k_{5d}\frac{c_{5,k}^{cell}(t)}{d}L_{pe}\Delta H_{pe}-2k_{2d}\frac{c_{2,k}^{cell}(t)}{d}L_{pe}\Delta H_{pe}-k_{3d}\frac{c_{3,k}^{cell}(t)}{d}L_{pe}\Delta H_{pe}
\end{aligned}
\tag{5}
$$

At discharging:

$$
\eta_c=\eta_c^{+}+\eta_c^{-}=\frac{RT}{nF}\left[\ln\left(\frac{c_{2,mean}^{cell}+\frac{i}{nFk_{2m}}}{c_{2,mean}^{cell}}\frac{c_{5,mean}^{cell}+\frac{i}{nFk_{5m}}}{c_{5,mean}^{cell}}\right)\right] \tag{16}
$$

where $k_{im}(i=2,..,5)$ represent the mass transfer coefficients which are shown as following[3]:

$$
k_{im}=7\frac{k_i\epsilon^{1.5}}{d_f}\left(\frac{\rho d_f}{\mu^{+/-}}\right)^{0.4}v_{pe}^{0.4} \tag{17}
$$

where $k_i(i=2,..,5)$ represents the measured diffusion coefficient of vanadium species which is related to the porosity of electrode[32], ρ is the density of electrolyte, and v_{pe} is the velocity of electrolyte in the porous electrode, as shown in Eq. (18).

$$
v_{pe}=\frac{Q}{\epsilon A_{cs}} \tag{18}
$$

According to Eq. (18), the concentration overpotential is related to both the electrode fiber diameter and the electrolyte flow rate. In addition, the electrode fiber diameter also affects the activation overpotential which can be derived from Butler-Volmer expressions[33, 34]:

$$
\begin{aligned}
i^{+} &= \epsilon aFk^{+}\left(c_4^{tank}\right)^{\alpha_2^{-}}\left(c_5^{tank}\right)^{\alpha_2^{+}}\left[\exp\left(\frac{\alpha_2^{+}F\eta_a^{+}}{RT}\right)-\exp\left(\frac{-\alpha_2^{-}\eta_c^{+}}{RT}\right)\right]\\
i^{-} &= \epsilon aFk^{-}\left(c_2^{tank}\right)^{\alpha_1^{+}}\left(c_3^{tank}\right)^{\alpha_1^{-}}\left[\exp\left(\frac{\alpha_1^{+}F\eta_a^{-}}{RT}\right)-\exp\left(\frac{-\alpha_1^{-}\eta_c^{-}}{RT}\right)\right]
\end{aligned}
\tag{19}
$$

where a is the specific surface area which can be estimated by Carla's model[35] as shown in Eq. (20), $\alpha_1^{\pm}/\alpha_2^{\pm}$ represent the apparent transfer coefficients for the electrochemical reactions in Eq. (1) and Eq. (2). For equal apparent transfer coefficients of 0.5, the activation overpotential can be derived from Eq. (21) according to Eq. (19).

$$
a=4\frac{1-\epsilon}{d_f} \tag{20}
$$

$$
\begin{aligned}
\eta_a^{-} &= \frac{2RT}{nF}\sinh^{-1}\left(\frac{i}{\epsilon ak^{-}F\sqrt{c_2^{tank}c_3^{tank}}}\right)\\
\eta_a^{+} &= \frac{2RT}{nF}\sinh^{-1}\left(\frac{i}{\epsilon ak^{+}F\sqrt{c_4^{tank}c_5^{tank}}}\right)
\end{aligned}
\tag{21}
$$

where $k^{\pm}$ represents the reaction rate constant which is a temperature dependent variable. Moreover, $k^{\pm}$ at the current temperature can be calculated from Eq. (22)[36] according to the reference value given in Table A1.

$$
\begin{aligned}
k^{-} &= k_{ref}^{-}\cdot\exp\left(\frac{-FE_0^{-}}{R}\left[\frac{1}{T_{ref}}-\frac{1}{T}\right]\right)\\
k^{+} &= k_{ref}^{+}\cdot\exp\left(\frac{FE_0^{+}}{R}\left[\frac{1}{T_{ref}}-\frac{1}{T}\right]\right)
\end{aligned}
\tag{22}
$$

In order to verify the accuracy of our established model, we perform a simulation verification according to the parameters adopted in [33]. The simulated charge/discharge voltage curves are compared with the experimentally measured charge/discharge voltage curves at a current density of $10Am^{-2}$ and SOC_{min} of 10% and SOC_{max} of 90% as mentioned in [33], as shown in Fig. 1. The simulated charge/discharge voltage curves are in good agreement with the experimental results in terms of both shapes and values. The voltage is related to the ion concentration in the positive and negative half-cells, and by comparing the voltage change, it can reflect the ion concentration change in the model. This shows that the model has good accuracy and can support the next parameter optimisation experiments.

2.4. Simulation results and discussion

In order to establish an accurate optimisation model of electrolyte flow rate and electrode fibre diameter, it is crucial to identify the performance of VRFB under different conditions. Therefore, it is required to precisely quantify the effects of electrolyte flow rate and electrode fibre diameter on the capacity attenuation and voltage loss of VRFB. However, the resulting electrochemical model is extremely complex, making highly challenging the analysis of the effect of flow rate and electrode fiber diameter on the VRFB performance. Therefore, we analyse the influence of electrolyte flow rate and electrode fibre diameter on the performance of VRFB from the perspective of simulation results combined with the electrochemical model. The parameters used in the simulation are shown in Table A2.

We use the CCCV procedure to simulate, and the charging and discharging current are shown in Fig. 2. The range of charging and discharging is subject to the state of charge(SOC), with the lower limit of 10% and the upper limit of 90%. It means that the SOC of any half-cell is not allowed to cross the threshold. Meanwhile, the initial concentration of V^{2+}/V^{5+}

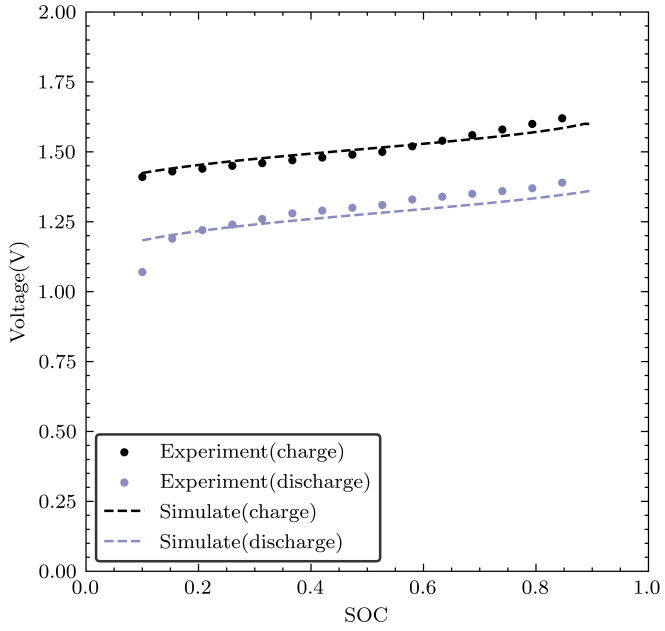

Figure 1: A comparison of simulated and experimentally measured charge-discharge curves

is $0.1 mol/L$ and V^{3+}/V^{4+} is $0.9 mol/L$. Then, capacity decay and voltage loss are discussed under the condition that the electrolyte flow rate is 2 cm^3/min and the electrode fibre diameter is 17.6 μm.

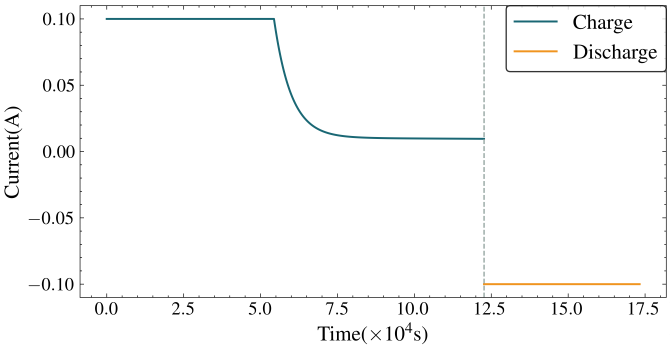

Figure 2: Charging and discharging current

2.4.1. *Quantification of capacity decay*

In general, the remaining capacity of VRFB is defined as the amount of charge that can be discharged. According to Eq. (1) and Eq. (2), it is closely associated with each ion's amount in the half-cells. Therefore, the source of capacity decay is the ion variation brought about by ion transmembrane transfer. As shown in Fig. 3, ions transfer shows a trend of violent fluctuations during charging and discharging. However, as shown in the points representing the end of a cycle in Fig. 3, it is evident that the total ion content of the positive half-cell shows an upward trend. According to Eq. (5), we can find that the ion transfer velocity is mainly bonded to ion concentration and ion transfer coefficient. During the charging and discharging cycles, the ion diffusion coefficient is constant, but the ion concentration is constantly changing, which leads to different degrees of diffusion of different ions in different processes of charging and discharging. During the charging process, the concentration of V^{2+} in the positive half-cell increases and the concentration of V^{3+} decreases, so the ion diffusion is mainly dominated by V^{2+}, while the concentration of V^{5+} in the negative half-cell increases and the concentration of V^{4+} decreases. Since the diffusion coefficient of V^{2+} is larger than that of V^{5+}, more ions from the positive half-cell diffuse to the negative half during charging. The discharging phase is similar to the charging phase, and since the diffusion coefficient of V^{3+} is smaller than that of V^{4+}, more ions from the negative half of the cell diffuse into the positive half during the discharging phase. The above leads to fluctuations in the amount of positive and negative half-cell ions. Since the diffusion coefficient of ions in the positive half-cell is overall smaller than that in the negative half-cell, and due to the self-discharge reaction, the V^{3+} ions, which have the smallest diffusion coefficient, will gradually increase. This leads to the gradual transfer of ions from the negative half-cell to the positive half-cell.

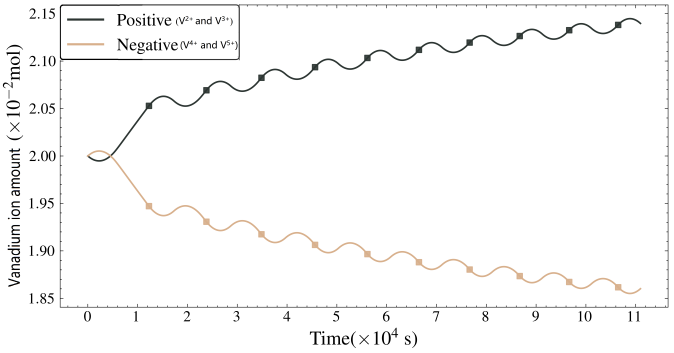

Figure 3: Trends in the amount of vanadium ions in each half-cell during the early cycles

To facilitate the analysis of vanadium ion transfer throughout the simulation, we plot the trends and the rate of change of the amount of vanadium ions in each half-cell. According to Fig. 4 and Fig. 5, the vanadium ions of the negative half-cell transfer to the positive half-cell at a breakneck speed in the early stage of the charging-discharging cycles. Then the ion transfer velocity decreases rapidly until the ion transfer rate between the half-cells remains relatively stable. It also means that the remaining capacity of VRFB presents a decaying trend from fast to slow.

As shown in Fig. 6, in the first ten cycles, the change of V^{4+} is the most obvious, and it remains at a high state during the charging-discharging cycle. The diffusion coefficient of the positive half-cell ions is smaller than the diffusion coefficient of the negative half-cell ions.Therefore, when the concentrations of the positive and negative half-cell ions are similar, the ions in the negative half-cell are gradually transferred to the positive half-cell. . As the vanadium ion concentration changes, ion diffusion between the two half-cells is gradually balanced. Therefore, the velocity of vanadium ion transfer tends to be zero, as shown in Fig. 5. However, after the equilibrium point of ion dif-

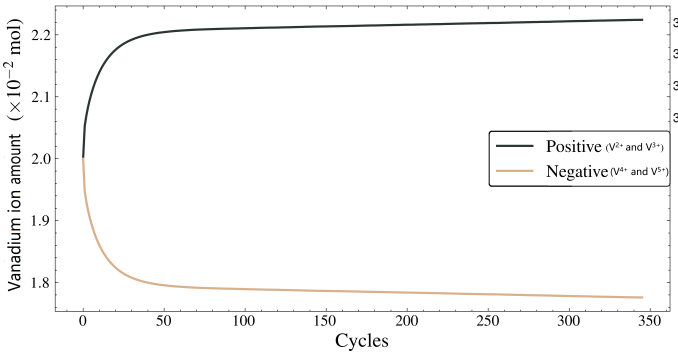

Figure 4: Trends in the amount of vanadium ions in each half-cell during long-term cycling

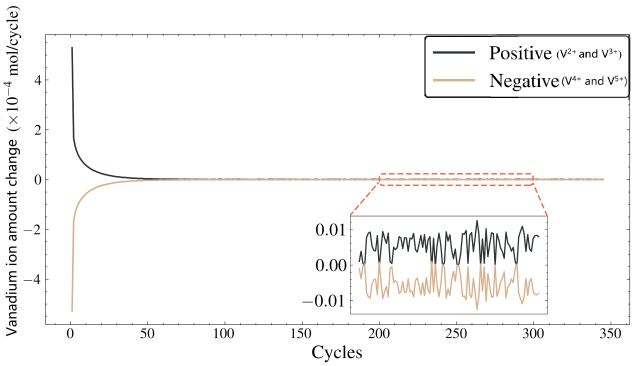

Figure 5: Rate of change of vanadium ion amount in each half-cell during long-term cycling

fusion is reached, there still exists electrolyte transfer between the two half-cells, as shown in Fig. 7. It alters the concentration of vanadium ions, disrupting the ion diffusion's balance. Therefore, the vanadium ions still diffuse from the negative half-cell to the positive half-cell at a minimal rate. Therefore, at the early stage of charging and discharging cycles, the main source of capacity decay is the difference in ion diffusion coefficients. The capacity decay due to electrolyte transmembrane loss, which is related to the electrode fibre diameter and electrolyte flow rate, can only be better observed during the long-term charging and discharging cycles.

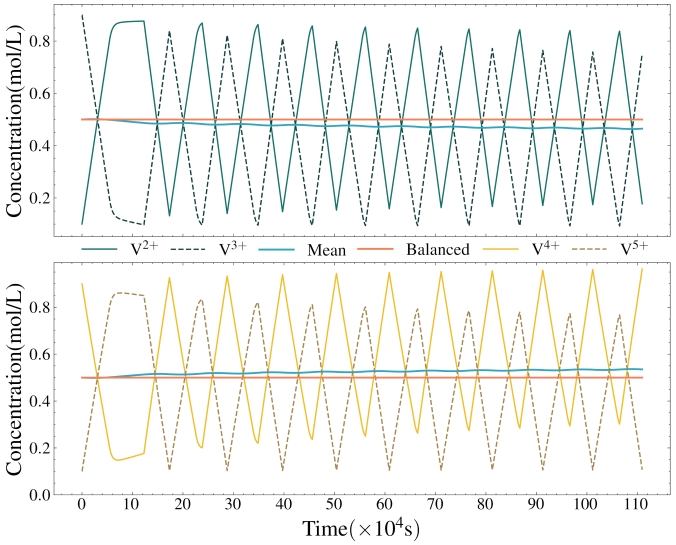

Figure 6: Variation of different vanadium ion concentrations in each half-cell

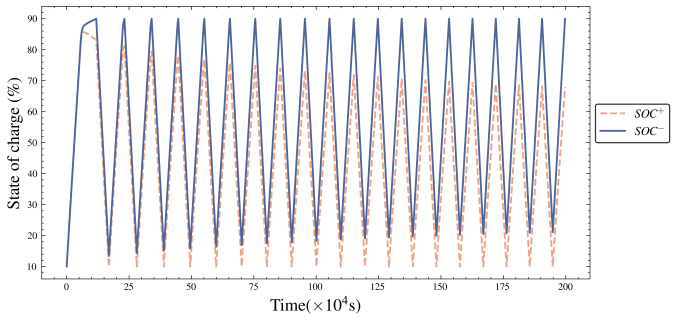

Figure 7: SOC variation curve of each half-cell

Analysis shows that the capacity decay, which corresponds with the vanadium ions amount, is mainly affected by the difference in the ion diffusion coefficients in the early cycle. In the long-term cycles, the electrolyte transfer affected by the electrolyte flow rate and the electrode fibre diameter becomes the main factor impacting the capacity decay. In addition, we need to further quantify the capacity fade according to the SOC variation of VRFB. The SOC of two half-cells is defined as follows:

$$SOC^{+} = \frac{c_5^{tank}}{c_4^{tank} + c_5^{tank}}$$
$$SOC^{-} = \frac{c_2^{tank}}{c_2^{tank} + c_3^{tank}} \quad (23)$$

As shown in Fig. 7, when we run the simulation loop with a fixed upper and lower SOC limit, the SOC of the positive half-cell reaches the lower bound. It means that there is not enough V^{5+} left to support the reaction when the SOC constraint is satisfied. In other words, it is the concentration of V^{5+} in the positive half-cell that limits the discharge process. Although the vanadium ions in the negative half-cell are still able to support the reaction, the reaction cannot proceed due to the limit of V^{5+}. And the SOC of the negative half-cell reaches the upper bound in the charge process. It means that there is not enough V^{3+} left to support the reaction when the SOC constraint is satisfied. In other words, it is the concentration of V^{3+} in the negative half-cell that limits the charge process. Although the vanadium ions in the positive half-cell are still able to support the reaction, the reaction cannot proceed due to the limit of V^{3+}. Therefore, V^{5+} and V^{3+} are the short boards of the positive and negative half-cells, respectively, which limit the charge and discharge process. That is, the maximum available capacity of VRFB is mainly influenced by the amount of V^{3+} and V^{5+}. Therefore, we can use the sum of the amount of V^{3+} and V^{5+} to represent the maximum available capacity. Further, we define the state of health (SOH) as the ratio of the remaining reactive ions to the initial ions, as shown in Eq. (24), to quantify the maximum available capacity of VRFB. Moreover, capacity decay is the difference between the initial SOH and the current SOH.

$$SOH = \frac{c_3^{tank} V_{tank}^{-} + c_5^{tank} V_{tank}^{+}}{\left(c_4^{init} + c_5^{init}\right) V} \times 100\% \quad (24)$$

2.4.2. *Quantification of voltage loss*

The voltage loss of VRFB is also closely related to the change in ion concentration. We quantify voltage loss by analyzing each component of the voltage according to Eq. (13), including open circuit voltage, concentration overpotential, activation overpotential and ohmic voltage drop.

As shown in Fig. 8 and Fig. 9, the open circuit voltage gradually fails to reach the set upper voltage over long cycles. Eq. (14) states that the open circuit voltage is related to vanadium ion concentrations. Then, we use the vanadium ion concentration in the tank $c_i^{tank} (i = 2, 3, 4, 5)$ as an approximate proxy for the average vanadium ion concentration in the half-cell $c_{i,mean}^{cell} (i = 2, 3, 4, 5)$. According to Eq. (14) and Eq. (23), we rewrite it as the expression related to SOC, as shown in Eq. (25). According to Fig. 7, when the SOC of the positive half-cell reaches the upper limit of the SOC, it is found that the SOC of the negative half-cell decreases with time. According to Eq. (25), it can be concluded that as the difference in vanadium ion concentration between the half-cells increases, the maximum value of the open circuit voltage decreases. Moreover, the loss of open circuit voltage is not a factor affecting the system's efficiency of the VRFB, but more of a factor reflecting the health of the VRFB, similar to the capacity decay. They both decay with the imbalance of vanadium ion concentration between the half-cells. Therefore, we can increase the maximum open-circuit voltage by reducing the capacity decay, so the open-circuit voltage is no longer considered in the scope of voltage loss.

$$E_{OCV} = E_0^{'} + \frac{RT}{nF} \ln\left(\frac{1}{\left(\frac{1}{SOC^{+}} - 1\right)\left(\frac{1}{SOC^{-}} - 1\right)}\right) \quad (25)$$

Ohmic voltage drop is only connected to current density and resistivity, so it is not considered when optimizing the electrolyte flow rate and electrode fibre diameter. According to Eq. (13), in addition to the ohmic voltage drop, there is concentration overpotential and activation overpotential that causes voltage loss, reducing the energy conversion efficiency of VRFB. Therefore, we define the voltage loss as the sum of the concentration overpotential and the activation overpotential over the simulation period. For ease of calculation, we average it as an indicator of voltage loss, as shown in Eq. (26).

$$V_{loss} = \frac{\sum_{t=0}^{t_{end}} \left(\eta_a^{+} + \eta_a^{-} + \eta_c^{+} + \eta_c^{-}\right)}{t_{end}} \quad (26)$$

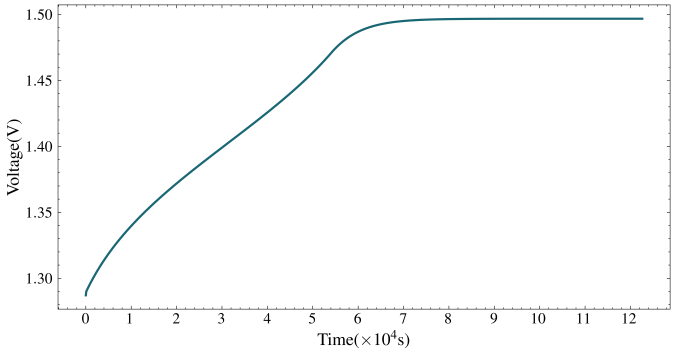

Figure 8: Open-circuit voltage in the first cycle

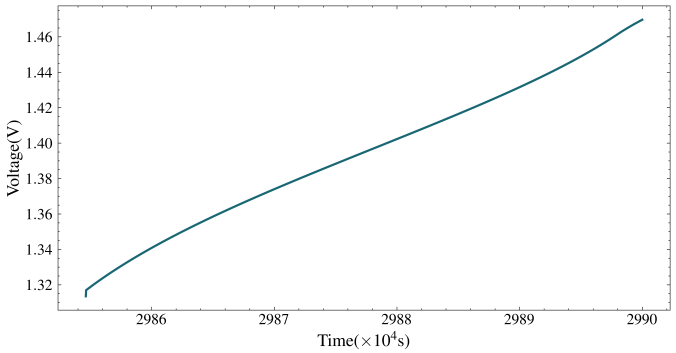

Figure 9: Open-circuit voltage in the last cycle

We have quantified the capacity decay and voltage loss through the above analysis. Next, we must determine the electrolyte flow rate and electrode fibre diameter effects on voltage loss and capacity fade. Therefore, we conduct further analysis through the simulation results of four different electrolyte flow rates and electrode fibre diameters.

2.4.3. *Effect of electrolyte flow rate*

This section conducts a simulation under the condition of constant electrode fibre diameter and different electrolyte flow rates. According to Fig.10, the SOH under different conditions decreased rapidly to 80% in the early stage of simulation. Then, it falls steadily at a low rate. Although as mentioned earlier, the early capacity decay mainly comes from the difference in the ion diffusion coefficients. It should not be taken into account in capacity decay. However, it is evident from Fig. 10 that the turning points of all curves are basically the same. Accordingly, we assume that the capacity decay caused by the difference in ion transfer coefficients can be regarded as the same for different electrolyte flow rates. Moreover, the gap of capacity decay caused by different electrolyte flow rates is gradually reflected after the turning point. In addition, the greater the electrolyte flow rate, the more significant the capacity decay.

At the same time, Fig. 11 shows the same voltage loss trend as capacity decay. The variation of voltage loss has also experienced a process from fast to smooth. However, it is evident that the greater the electrolyte flow rate, the less significant the voltage loss. Therefore, the effect of electrolyte flow rate on capacity decay and voltage loss is the opposite.

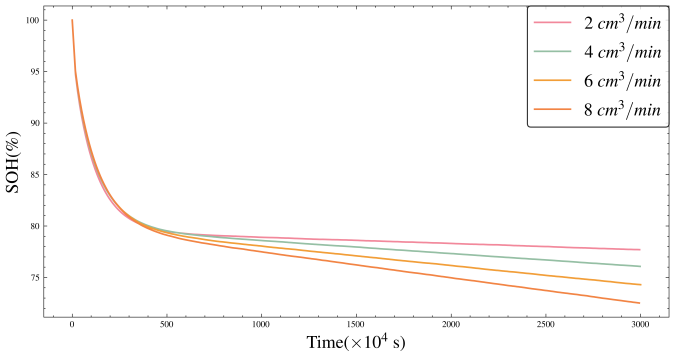

Figure 10: SOH at the minimum SOC under different electrolyte flow rates

2.4.4. *Effect of electrode fiber diameter*

This section conducts a simulation with a constant electrolyte flow rate and different electrode fibre diameters. According to Fig.12, similar to the electrolyte flow rate, the variation trend of SOH affected by the electrode fibre diameter is also from swift to smooth. Furthermore, the inflexion points of all curves are almost at the same position. It shows that the capacity decay caused by ion diffusion coefficients is the same for different electrolyte flow rates and electrode fibre diameters. Therefore, using the SOH at the end of the simulation is feasible to measure the capacity fade caused by the electrolyte flow rate and the electrode fibre diameter. Unlike Fig. 10, the difference in SOH becomes insignificant at larger electrode fibre diameters, and a small electrode fibre diameter result in large capacity decay.

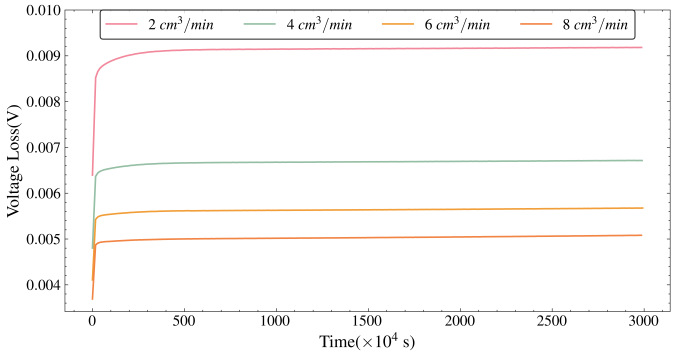

Figure 11: SOH at the minimum SOC under different electrolyte flow rates

According to Fig. 13, it is evident that the greater the electrode fibre diameter, the more significant the voltage loss. Like the effect of electrolyte flow rate, the effect of electrode fibre diameter on capacity decay and voltage loss is also inconsistent.

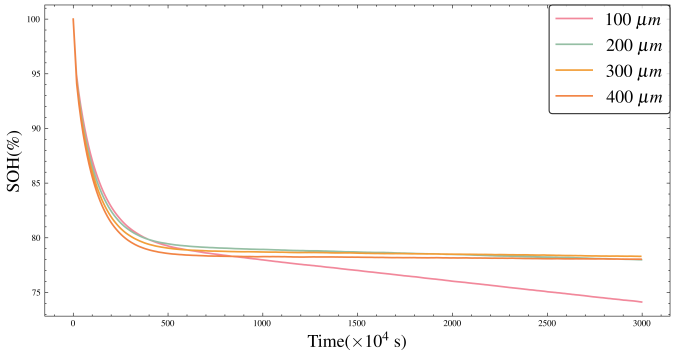

Figure 12: SOH at the minimum SOC under different electrode fiber diameter

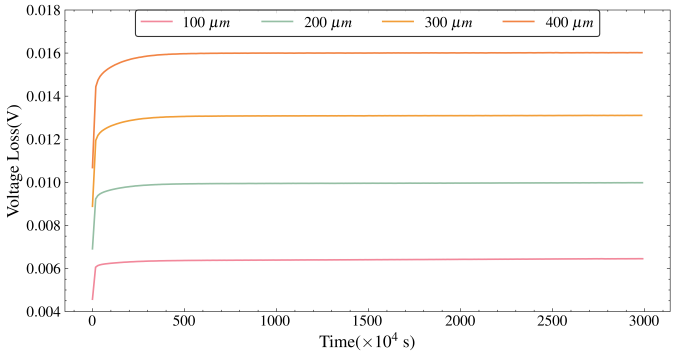

Figure 13: Voltage at the minimum SOC under different electrode fiber diameter

3. Optimization of electrolyte flow rate and electrode fiber diameter

3.1. *Multi-objective optimization modeling*

According to Section 2, a higher electrolyte flow rate will increase the volume loss of VRFB, resulting in more significant

capacity decay. However, a higher electrolyte flow rate will reduce the voltage loss caused by concentration overpotential. Similarly, a larger electrode fiber diameter will give rise to more significant voltage loss, and a smaller fiber diameter can reduce the volume loss, thus mitigating capacity decay. This is a multi-objective optimization problem with voltage loss and capacity decay objectives. The general approach is to assign different weights to these two objectives to transform the problem into a single objective optimization problem. However, this method is not suitable for voltage loss and capacity decay. First of all, they have different dimensions. Secondly, they have significant numerical differences. Therefore, it is not easy to set appropriate weights to obtain a satisfactory solution. In order to avoid this problem, this study proposes a multi-objective optimization framework to optimize the voltage loss and capacity decay of VRFB simultaneously. In this framework, the two objectives is defined as follows:

$$\begin{aligned} f_1 &= f_v(d_f, Q) = \sum_{t=0}^{t_{end}} (\eta_a^+ + \eta_a^- + \eta_c^+ + \eta_c^-) \Big| t_{end} \\ f_2 &= f_c(d_f, Q) = \mathrm{SOH}_{end} \end{aligned} \tag{27}$$

The objective of this study is to obtain the minimum voltage loss and capacity decay. Furthermore, the multi-objective optimization model can be expressed as follows:

$$\begin{cases} \max F(d_f, Q) = \left[\frac{1}{f_v(d_f, Q)}, f_c(d_f, Q) \right]^T \\ \text{s.t.} \\ d_{f,min} \le d_f \le d_{f,max} \\ Q_{min} \le Q \le Q_{max} \\ \mathrm{SOC}_{min} \le \mathrm{SOC} \le \mathrm{SOC}_{max} \\ |I| \le I_{max} \end{cases} \tag{28}$$

3.2. Multi-objective optimization framework

For multi-objective problems, multiple objectives are in conflict with each other. It is generally impossible to reach the optimal state at the same time. Therefore, it is impossible to find an absolute optimal solution directly, so the concept of Pareto optimality is introduced. A series of non-inferior solutions can be found in the solution space, which means that it is impossible to find a solution that is superior to it in every objective. All these non-inferior solutions constitute the Pareto frontier of the problem.

In this study, the meta-heuristic algorithm is used to generate the non-inferior solution. It relies on random and local search algorithms to generate new solutions and selects non-inferior solutions according to the fitness function. In order to distribute the non-inferior solution evenly, the crowding strategy is added when choosing the non-inferior solution. The overall algorithm flow is as follows:

Because it is not easy to directly obtain the two objectives from the electrochemical model, an optimization framework based on Pareto optimality combined with simulation and meta-heuristic algorithms is proposed. In this study, the electrochemical simulation model is established by Dymola, and then the communication between Python and Dymola is established.

Algorithm 1: Multi-objective meta-heuristic algorithm

Input: Parameter constraint and fitness function
Output: Uniformly distributed Pareto frontier

```
P ←Initialization solution set;
for i = 1 to cycle do
    Q ←Using random algorithms or local search to
      generate a new solution set;
    R ←Combine P and Q to get the solution set;
    Obtain the fitness values of all solutions in R;
    P ←The solution set updated according to the
      dominance relation and crowding degree
end
```

The fitness is calculated through the simulation results of Dymola output. Take the Fast Non-dominated Sorting Genetic Algorithm (NSGA-II) as an example, and the specific algorithm framework is shown in Fig. 14. The algorithmic framework is in a continuous computational loop until the algorithm termination condition is reached. A single computational loop can be divided into three phases. In the first phase, NSGA-II is responsible for parameter crossing and mutation. New parameters are obtained to extend the search space of the parameters from the original ones. The goal is to find a better solution that satisfies the constraints. In the second stage, the NSGA-II algorithm passes the parameters to Dymola for simulation to obtain the capacity decay and voltage loss under these conditions. In the third step, we feed the obtained capacity decay and voltage loss into NSGA-II to calculate the fitness function. Based on the fitness function and the Pareto principle, the parameters with higher fitness are selected for the next cycle.

There is no dominant relationship between the solutions in the Pareto frontier, meaning that it is impossible to determine a specific solution through the two objectives. Therefore, this study uses the sensitivity ratio-based method proposed by Wang[37] to select the most cost-effective solution quantitatively. The specific steps are as follows:

1. Suppose the Pareto frontier as X. The average variability of each non-dominated solution is obtained from Eq. (29).

$$\begin{aligned} k_1^m &= \frac{1}{2}\left(\frac{f_2^m - f_2^{m-1}}{f_1^m - f_1^{m-1}} + \frac{f_2^{m+1} - f_2^m}{f_1^{m+1} - f_1^m} \right) \\ k_2^m &= \frac{1}{2}\left(\frac{f_1^m - f_1^{m-1}}{f_2^m - f_2^{m-1}} + \frac{f_1^{m+1} - f_1^m}{f_2^{m+1} - f_2^m} \right) \end{aligned} \tag{29}$$

2. The sensitivity ratio for each non-dominated solution is calculated as the ratio of the average variability to the value of the objective function, as shown in Eq. (30).

$$\begin{aligned} \delta_1^m &= \frac{k_1^m}{f_1^m} \\ \delta_2^m &= \frac{k_2^m}{f_2^m} \end{aligned} \tag{30}$$

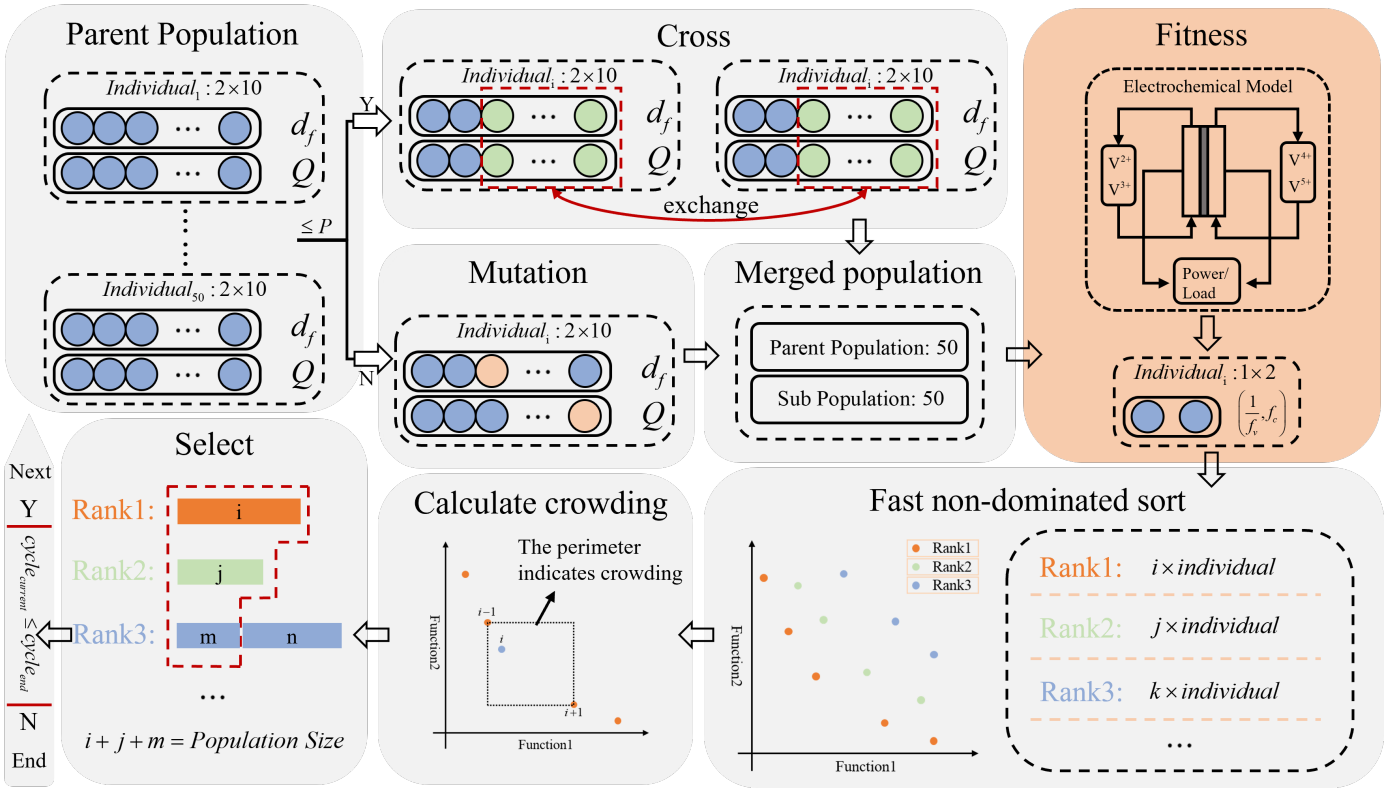

Figure 14: Algorithm framework of NSGA-II combined with simulation

3. The sensitivity ratio indicates the sensitivity of the average variability with the objectives. In order to facilitate the follow-up comparison, it needs to be dimensionless, as shown in Eq. (31).

$$\varepsilon_1^m = \frac{\delta_1^m}{\sum_{i=1}^{M} \delta_1^i}$$
$$\varepsilon_2^m = \frac{\delta_2^m}{\sum_{i=1}^{M} \delta_2^i} \quad (31)$$

4. Selection of non-dominant solution set X^* based on sensitivity ratio, which is defined as Eq. (32).

$$X^* = \{x^i \in X | \nexists x^j \in X, \varepsilon_1^j > \varepsilon_1^i \ \& \varepsilon_2^j > \varepsilon_2^i\} \quad (32)$$

5. Calculate the degree of bias ω for different objective functions, and the value range is $(0, 1)$. As shown in Eq. (33), ω_1 and ω_2 are the bias degrees of the non-inferior solution based on sensitive ratios for objective functions f_1 and f_2, respectively.

$$\omega_1^m = \frac{\varepsilon_1^m}{\varepsilon_1^m + \varepsilon_2^m}$$
$$\omega_2^m = \frac{\varepsilon_2^m}{\varepsilon_1^m + \varepsilon_2^m} \quad (33)$$

6. Calculate the difference in sensitivity ratio $\Delta\varepsilon^m$, as shown in Eq. (34). The smallest $\Delta\varepsilon^m$ corresponds to the solution least affected by the change of the objective values.

$$\Delta\varepsilon^m = |\varepsilon_1^m - \varepsilon_2^m| \quad (34)$$

3.3. Optimization results

In order to ensure that the simulation results are only affected by the electrode fiber diameter and the electrolyte flow rate, the SOC_{min} and SOC_{max} in Eq. (24) are 10% and 90% respectively. Furthermore, in this study, a constant current of is adopted for the charge-discharge cycle to verify the proposed method. It ensures the same charge variation in the same simulation duration. In addition, other parameters are consistent with Table A2.

This study assumes that the electrolyte flow rate is between 1 ~ 10cm^3/min and the electrode fiber diameter is between 1 ~ 100μm . In this study, the electrolyte flow rate is accurate to one decimal place, and the electrode fiber diameter is accurate to two decimal places. Based on the proposed framework, the distribution of the Pareto frontier was obtained, and the solutions in the Pareto frontier were numbered consecutively, as shown in Fig. 16. Then, based on the obtained Pareto frontier, we used the sensitivity ratio-based method for further analysis.

Firstly, the sensitivity ratios of the non-inferior solutions for f_1 and f_2 were calculated. Then, we represent the dominance relationship between the sensitivity ratios in Fig. 15. Thus, based on the dominance relationship of sensitivity ratios of the 100 Pareto non-inferior solutions, 89 solutions have been ruled out. The remaining solutions constitute a non-inferior solution set based on sensitive ratios, as shown in red.

We have screened about a fifth of the non-inferior solutions to facilitate the selection. Then, the quantized value of the bias degree for every objective function is shown in Fig. 16. ω_1

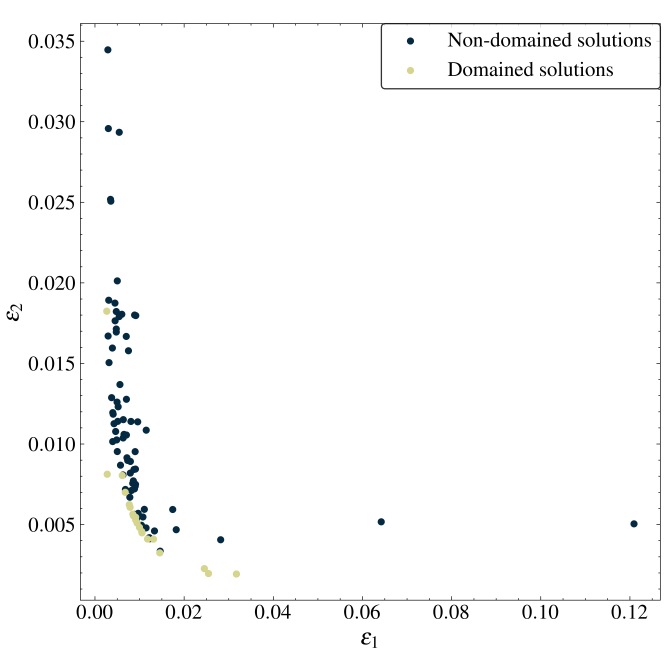

(a) The distribution based on sensitivity ratios.

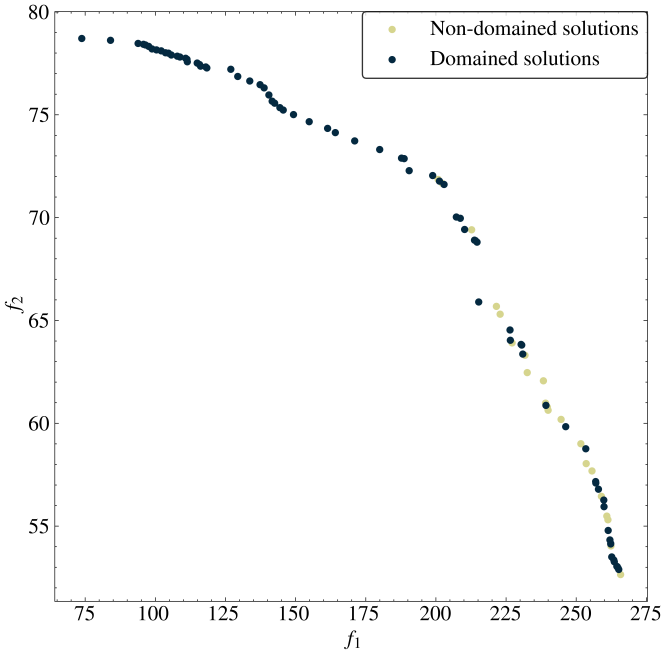

(b) The distribution of sensitivity ratios in Pareto frontier.

Figure 15: The distribution of non-inferior solutions based on sensitive ratios and its distribution in Pareto frontier.

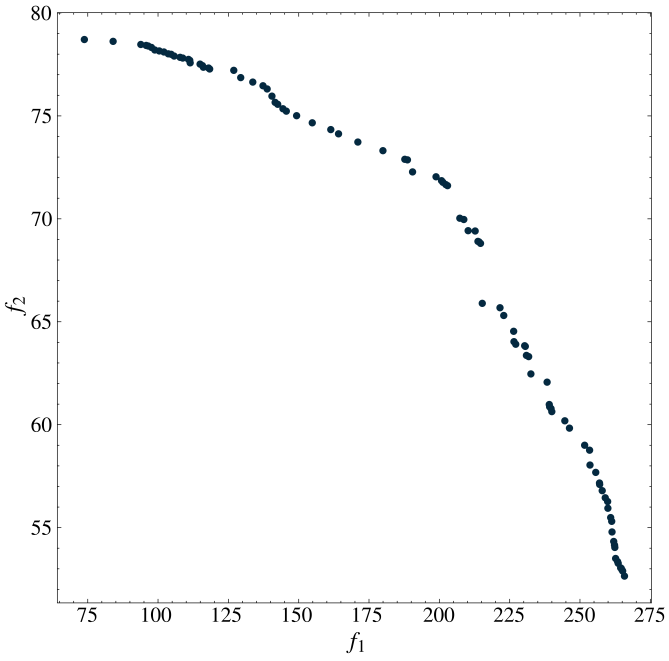

Figure 16: Pareto frontier

and ω_2 are the bias degrees of the Pareto non-inferior solution for objective functions f_1 and f_2, respectively. That is the bias degree of the voltage loss and capacity fading of VRFB under this condition. For example, the solutions numbered 23, 28 and 29 have ω_1 greater than ω_2, so they are more biased towards voltage loss. In contrast, the solutions numbered 0 and 69 have ω_1 less than ω_2, so they are more biased towards capacity decay. The decision-makers can balance and select more effectively based on these quantitative indicators.

Moreover, if the two objective functions are considered equally, we can select a good unbiased solution based on delta. As shown in Fig. 18, the 17th solution is determined to be the unbiased and good solution acceptable for the objectives f_1 and f_2. Finally, we obtain an unbiased and good solution to optimize the voltage loss and capacity decay in VRFB where the electrode fiber diameter is $107\mu m$ and the electrolyte flow rate is $9.2cm^3/min$. The capacity decay during simulation is 42.32% and the average voltage loss is $0.004V$ under this condition.

4. Conclusion

This study proposes physics-based simulation combined multi-objective optimization approach for reduction of both capacity decay and voltage loss of Vanadium redox flow battery. The main objective of this approach is to find the optimal values of electrolyte flow rate and electrode fiber diameter while minimizing capacity decay and voltage loss.

Firstly, this study quantifies and analyses the effects of electrolyte flow rate and electrode fiber diameter on capacity decay and voltage loss through simulation. It is proved that the electrolyte flow rate and the electrode fiber diameter not only affect

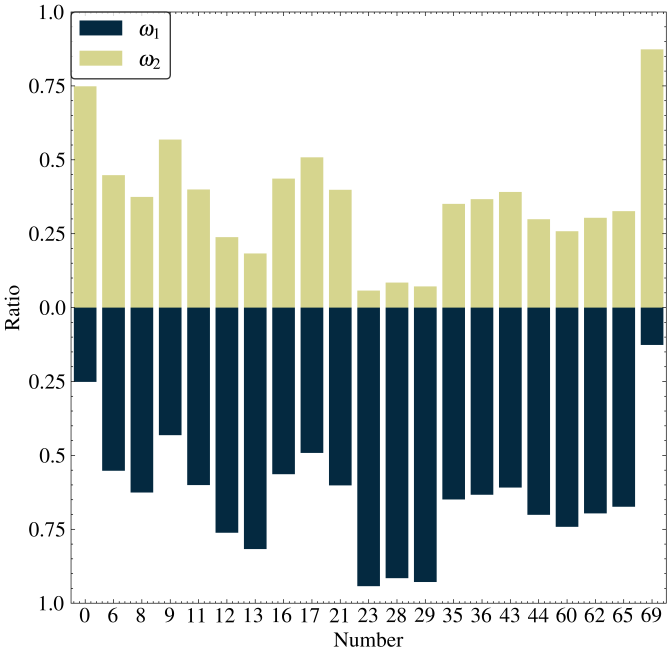

Figure 17: The bias degree of solutions to f_1 and f_2.

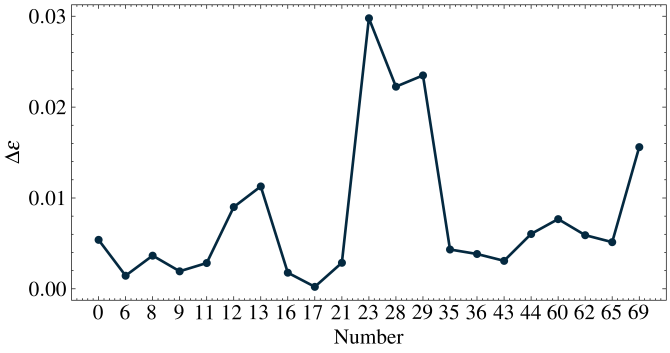

Figure 18: The distribution of the absolute value difference of the sensitivity ratio.

the capacity decay and voltage loss but also have the opposite effect. It means that the two objectives cannot be optimized simultaneously.

Therefore, this study uses a multi-objective meta-heuristic algorithm to solve the Pareto frontier of the problem. The simulation results are used to replace the standard fitness calculation. The sensitivity ratio is introduced to select a better solution effectively.

Meanwhile, the proposed VRFB optimization framework is flexible. The electrochemical parameters can be adjusted according to practical needs. Additionally, the electrolyte flow rate and electrode fiber diameter ranges are free to choose.

In addition, future research can focus on ion concentration initialization design. When analyzing the available capacity of VRFB, it is found that the balanced initialization will lose a sizeable available capacity in the early cycles due to the difference in the diffusion coefficient. Moreover, when the ion concentration and diffusion rate reach equilibrium, the capacity decay rate decreases significantly. Therefore, how to design the initial ion concentration of VRFB to obtain higher available capacity and a slower capacity decay rate is worth studying.

References

[1] M. Skyllas-Kazacos, M. Rychcik, R. G. Robins, A. G. Fane, M. A. Green, New all-vanadium redox flow cell, Journal of the Electrochemical Society 133 (1986) 1057. doi:10.1149/1.2108706.

[2] E. Sum, M. Skyllas-Kazacos, A study of the v(ii)/v(iii) redox couple for redox flow cell applications, Journal of Power Sources 15 (2) (1985) 179–190. doi:10.1016/0378-7753(85)80071-9.

[3] S. König, M. R. Suriyah, T. Leibfried, Validating and improving a zero-dimensional stack voltage model of the vanadium redox flow battery, Journal of Power Sources 378 (2018) 10–18. doi:10.1016/j.jpowsour.2017.12.014.

[4] M. Rychcik, M. Skyllas-Kazacos, Characteristics of a new all-vanadium redox flow battery, Journal of Power Sources 22 (1) (1988) 59–67. doi:10.1016/0378-7753(88)80005-3.

[5] Y. Li, M. Skyllas-Kazacos, J. Bao, A dynamic plug flow reactor model for a vanadium redox flow battery cell, Journal of Power Sources 311 (2016) 57–67. doi:10.1016/j.jpowsour.2016.02.018.

[6] M. Skyllas-Kazacos, Secondary batteries – flow systems — vanadium redox-flow batteries, in: J. Garche (Ed.), Encyclopedia ofElectrochemical Power Sources, Elsevier, Amsterdam, 2009, pp. 444–453. doi:https://doi.org/10.1016/B978-044452745-5.00177-5.
URL https://www.sciencedirect.com/science/article/pii/B9780444527455001775

[7] Q. Wu, Y. Lv, L. Lin, X. Zhang, Y. Liu, X. Zhou, An improved thin-film electrode for vanadium redox flow batteries enabled by a dual layered structure, Journal of Power Sources 410-411 (2019) 152–161. doi:10.1016/j.jpowsour.2018.11.020.

[8] T. Jirabovornwisut, A. Arpornwichanop, A review on the electrolyte imbalance in vanadium redox flow batteries, International Journal of Hydrogen Energy 44 (45) (2019) 24485–24509. doi:10.1016/j.ijhydene.2019.07.106.

[9] B. Li, Q. Luo, X. Wei, Z. Nie, E. Thomsen, B. Chen, V. Sprenkle, W. Wang, Capacity decay mechanism of microporous separator-based all-vanadium redox flow batteries and its recovery, ChemSusChem 7 (2) (2014) 577–584. doi:10.1002/cssc.201300706.

[10] M. Skyllas-Kazacos, L. Cao, M. Kazacos, N. Kausar, A. Mousa, Vanadium electrolyte studies for the vanadium redox battery—a review, ChemSusChem 9 (13) (2016) 1521–1543. doi:10.1002/cssc.201600102.

[11] Y.-S. Chou, S.-C. Yen, A. Arpornwichanop, B. Singh, Y.-S. Chen, Mathematical model to study vanadium ion crossover in an all-vanadium redox flow battery, ACS Sustainable Chemistry & Engineering 9 (15) (2021) 5377–5387. doi:10.1021/acssuschemeng.1c00233.

[12] A. Tang, J. Bao, M. Skyllas-Kazacos, Dynamic modelling of the effects of ion diffusion and side reactions on the capacity loss for vanadium redox flow battery, Journal of Power Sources 196 (24) (2011) 10737–10747. doi:10.1016/j.jpowsour.2011.09.003.

[13] R. Badrinarayanan, J. Zhao, K. J. Tseng, M. Skyllas-Kazacos, Extended dynamic model for ion diffusion in all-vanadium redox flow battery including the effects of temperature and bulk electrolyte transfer, Journal of Power Sources 270 (2014) 576–586. doi:10.1016/j.jpowsour.2014.07.128.

[14] K. W. Knehr, E. Agar, C. R. Dennison, A. R. Kalidindi, E. C. Kumbur, A transient vanadium flow battery model incorporating vanadium crossover and water transport through the membrane, Journal of The Electrochemical Society 159 (9) (2012) A1446. doi:10.1149/2.017209jes.

[15] C. Sun, J. Chen, H. Zhang, X. Han, Q. Luo, Investigations on transfer of water and vanadium ions across nafion membrane in an operating vanadium redox flow battery, Journal of Power Sources 195 (3) (2010) 890–897. doi:10.1016/j.jpowsour.2009.08.041.

[16] K. Oh, M. Moazzam, G. Gwak, H. Ju, Water crossover phenomena in all-vanadium redox flow batteries, Electrochimica Acta 297 (2019) 101–111. doi:10.1016/j.electacta.2018.11.151.

[17] T. Sukkar, M. Skyllas-Kazacos, Water transfer behaviour across cation exchange membranes in the vanadium redox battery, Journal of Membrane Science 222 (1) (2003) 235–247. doi:10.1016/S0376-7388(03)00309-0.

[18] T. Mohammadi, S. C. Chieng, M. Skyllas Kazacos, Water transport study across commercial ion exchange membranes in the vanadium redox flow battery, Journal of Membrane Science 133 (2) (1997) 151–159. doi:10.1016/S0376-7388(97)00092-6.

[19] D. You, H. Zhang, J. Chen, A simple model for the vanadium redox battery, Electrochimica Acta 54 (27) (2009) 6827–6836. doi:10.1016/j.electacta.2009.06.086.

[20] S. K. Murthy, A. K. Sharma, C. Choo, E. Birgersson, Analysis of concentration overpotential in an all-vanadium redox flow battery, Journal of The Electrochemical Society 165 (9) (2018) A1746. doi:10.1149/2.0681809jes.

[21] X. Ma, H. Zhang, C. Sun, Y. Zou, T. Zhang, An optimal strategy of electrolyte flow rate for vanadium redox flow battery, Journal of Power Sources 203 (2012) 153–158. doi:10.1016/j.jpowsour.2011.11.036.

[22] C. Blanc, A. Rufer, Optimization of the operating point of a vanadium redox flow battery, in: 2009 IEEE Energy Conversion Congress and Exposition, 2009, pp. 2600–2605. doi:10.1109/ECCE.2009.5316566.

[23] A. Tang, J. Bao, M. Skyllas-Kazacos, Studies on pressure losses and flow rate optimization in vanadium redox flow battery, Journal of Power Sources 248 (2014) 154–162. doi:10.1016/j.jpowsour.2013.09.071.

[24] X. Binyu, Z. Jiyun, L. Jinbin, Modeling of an all-vanadium redox flow battery and optimization of flow rates, in: 2013 IEEE Power & Energy Society General Meeting, 2013, pp. 1–5. doi:10.1109/PESMG.2013.6672599.

[25] S. König, M. R. Suriyah, T. Leibfried, Innovative model-based flow rate optimization for vanadium redox flow batteries, Journal of Power Sources 333 (2016) 134–144. doi:10.1016/j.jpowsour.2016.09.147.

[26] B. Khaki, P. Das, Voltage loss and capacity fade reduction in vanadium redox battery by electrolyte flow control, Electrochimica Acta 405 (2022) 139842. doi:10.1016/j.electacta.2022.139842.

[27] B. Jiang, L. Wu, L. Yu, X. Qiu, J. Xi, A comparative study of nafion series membranes for vanadium redox flow batteries, Journal of Membrane Science 510 (2016) 18–26. doi:10.1016/j.memsci.2016.03.007.

[28] A. Tamayol, F. McGregor, M. Bahrami, Single phase through-plane permeability of carbon paper gas diffusion layers, Journal of Power Sources 204 (2012) 94–99. doi:10.1016/j.jpowsour.2011.11.084.

[29] L. Hao, P. Cheng, Lattice boltzmann simulations of anisotropic permeabilities in carbon paper gas diffusion layers, Journal of Power Sources 186 (1) (2009) 104–114. doi:https://doi.org/10.1016/j.jpowsour.2008.09.086.
URL https://www.sciencedirect.com/science/article/pii/S037877530801882X

[30] Q. Xu, T. S. Zhao, C. Zhang, Effects of soc-dependent electrolyte viscosity on performance of vanadium redox flow batteries, Applied Energy 130 (2014) 139–147. doi:10.1016/j.apenergy.2014.05.034.

[31] S. Corcuera, M. Skyllas-Kazacos, State-of-charge monitoring and electrolyte rebalancing methods for the vanadium redox flow battery, Eur. Chem. Bull. 1 (12) (2012) 511–519.

[32] B. Tjaden, S. J. Cooper, D. J. Brett, D. Kramer, P. R. Shearing, On the origin and application of the bruggeman correlation for analysing transport phenomena in electrochemical systems, Current Opinion in Chemical Engineering 12 (2016) 44–51. doi:10.1016/j.coche.2016.02.006.

[33] M. Vynnycky, Analysis of a model for the operation of a vanadium redox battery, Energy 36 (4) (2011) 2242–2256. doi:10.1016/j.energy.2010.03.060.

[34] A. K. Sharma, M. Vynnycky, C. Y. Ling, E. Birgersson, M. Han, The quasi-steady state of all-vanadium redox flow batteries: A scale analysis, Electrochimica Acta 147 (2014) 657–662. doi:10.1016/j.electacta.2014.09.134.

[35] R. Carta, S. Palmas, A. Polcaro, G. Tola, Behaviour of a carbon felt flow by electrodes part i: Mass transfer characteristics, Journal of Applied Electrochemistry 21 (9) (1991) 793–798. doi:10.1007/BF01402816.

[36] A. A. Shah, R. Tangirala, R. Singh, R. G. A. Wills, F. C. Walsh, A dynamic unit cell model for the all-vanadium flow battery, Journal of The Electrochemical Society 158 (6) (2011) A671. doi:10.1149/1.3561426.

[37] N. Wang, W.-j. Zhao, N. Wu, D. Wu, Multi-objective optimization: A method for selecting the optimal solution from pareto non-inferior solutions, Expert Systems with Applications 74 (2017) 96–104. doi:10.1016/j.eswa.2017.01.004.

[38] M. Gattrell, J. Park, B. MacDougall, J. Apte, S. McCarthy, C. W. Wu, Study of the mechanism of the vanadium 4+/5+ redox reaction in acidic solutions, Journal of The Electrochemical Society 151 (1) (2003) A123. doi:10.1149/1.1630594.

Appendix A.

Table A1: Reference values

Symbol	Description	Value	Unit	Source
E_0^+	Standard potential of positive reaction	-0.26	V	[36]
E_0^-	Standard potential of negative reaction	$+1.00$	V	[36]
k_{ref}^+	Positive reaction rate constant at reference temperature	3.56×10^{-6}	m/s	[36]
k_{ref}^-	Negative reaction rate constant at reference temperature	3×10^{-9}	m/s	[36]
T_{ref}	Reference temperature	293	K	[38]

Table A2: The parameters used in the simulation

Symbols	Quantity	Value	Unit
$V_{tank}^{+/-}$	Initial electrolyte volume in the tank	20	cm^3
L_pe	Length of the porous electrode	2.25	cm
W_pe	Width of the porous electrode	0.218	cm
H_pe	Height of the porous electrode	2.25	cm
N	Layers	60	1
r	Cell internal resistivity	2	Ωcm^2
n	Number of electrons transferred in the reaction	1	1
F	Faraday constant	96485	C/mol
R	Gas constant	8.314	$J/\left(mol \cdot K\right)$
$\frac{k_{2d}}{d}$	Diffusion coefficient of V^{2+}	3.17×10^{-8}	m/s
$\frac{k_{3d}}{d}$	Diffusion coefficient of V^{3+}	7.16×10^{-9}	m/s
$\frac{k_{4d}}{d}$	Diffusion coefficient of V^{4+}	2×10^{-8}	m/s
$\frac{k_{5d}}{d}$	Diffusion coefficient of V^{5+}	1.25×10^{-8}	m/s
ϵ	Electrode porosity	0.93	1
S_m	Membrane area	5×10^{-4}	m^2
θ	Membrane thickness	1.83×10^{-8}	m/s
κ_m	Membrane permeability	1.58×10^{-18}	m^2
k_2	Measured diffusion coefficient of V^{2+}	2.4×10^{-10}	m^2/s
k_3	Measured diffusion coefficient of V^{3+}	2.4×10^{-10}	m^2/s
k_4	Measured diffusion coefficient of V^{4+}	3.9×10^{-10}	m^2/s
k_5	Measured diffusion coefficient of V^{5+}	3.9×10^{-10}	m^2/s